Bayesian inference of particle source and sink in a closed-divertor using Balmer line spectroscopy

Bayesian inference of particle source and sink in a closed-divertor using Balmer line spectroscopy

OPEN ACCESS
IOP Publishing
Plasma Physics and Controlled Fusion
Plasma Phys. Control. Fusion **62** (2020) 085005 (14pp)
https://doi.org/10.1088/1361-6587/ab9732

Bayesian inference of particle source and sink in a closed-divertor using Balmer line spectroscopy

T Nishizawa[1,2], M Cavedon[1], F Reimold[2], R Dux[1], D Brida[1], H Wu[3], the EUROfusion MST1 team and the ASDEX Upgrade Team

[1] Max Planck Institute for Plasma Physics, Boltzmannstr. 2, 85748 Garching, Germany
[2] Max Planck Institute for Plasma Physics, Wendelsteinstr. 1, 17491 Greifswald, Germany
[3] NEMO Group, Dipartimento Energia, Politecnico di Torino, Corso Duca degli Abruzzi 24, 10129 Torino, Italy

E-mail: takashi.nishizawa@ipp.mpg.de

Received 20 January 2020, revised 5 May 2020
Accepted for publication 27 May 2020
Published 29 June 2020

Abstract

A new analysis technique for Balmer line spectroscopy that enables recombination rate (particle sink) and ionization rate (particle source) inference in a closed divertor configuration is reported. Bayesian inference is employed to systematically utilize all available information from multiple Balmer lines and constrain parameter ranges by using prior knowledge about plasmas. While a closed-divertor facilitates detachment, neutral plugging typically leads to large spatial variations in plasma parameters. A forward model is developed to take into account non-uniformity in the plasma parameters and applied to test data generated by divertor plasma simulations. It is shown that the forward model robustly provides particle source and sink inference over a wide parameter range. In addition, the precision improves as more Balmer lines are resolved simultaneously. The new analysis technique is also applied to an L-mode ASDEX Upgrade plasma in the high-recycling regime. The inferred quantities and their profiles are consistent with the expectations of a high-recycling divertor plasma. The further insight into the detachment physics will be provided by using this new analysis technique.

Keywords: detachment, spectroscopy, Bayesian inference

(Some figures may appear in colour only in the online journal)

1. Introduction

Mitigating heat load on a divertor target is considered as one of the critical challenges in achieving a commercial fusion reactor. If no counter measures are taken, a peak heat flux on the divertor target in ITER [1] will largely exceed the heat load limit of present-day materials. Fortunately, the divertor heat load can be reduced significantly through a process called 'detachment', leading to a tolerable heat flux [2, 3]. When detachment takes place, both electron temperature T_e and density n_e drop near the strike point and the plasma 'detaches' from the divertor target. However, the current understanding of the detachment process is mostly based on empirical laws and qualitative descriptions and the extrapolation of the detachment behavior to ITER and future reactors is not reliable. To this end, further study of the detachment processes through experiments, modeling and simulations is crucial for successful operations of ITER and future commercial fusion reactors.

Balmer line spectroscopy is a non-intrusive diagnostic technique and often used for characterizing divertor plasmas. Balmer lines are a spectral series of deuterium or its isotopes with wavelengths in the visible range, for which implementation of diagnositcs is relatively easy. Since many magnetic fusion experiments use mostly deuterium or its

isotopes for the main gas, Balmer line spectroscopy is often run routinely and a large set of atomic data is available. One of the plasma parameters Balmer line spectroscopy provides is n_e. When n_e is high ($\gtrsim 4\times10^{19}$ m^{-3}), the broadening of a $D_\epsilon(n=7\rightarrow2)$ line (H_ϵ for hydrogen) is dominated by Stark-broadening for a relatively cold divertor plasma. Fitting a D_ϵ spectrum by using a proper line-shape model provides n_e measurements [4, 5]. When other processes such as Zeeman effect and finite ion and neutral temperature are taken into account, n_e can also be measured from a $D_\delta(n=6\rightarrow2)$ line, or $D_\gamma(n=5\rightarrow2)$ line [4, 6, 7]. Another use of Balmer line spectroscopy is the detection of volume recombination [5, 8]. When recombination is present, the ratio of two Balmer line intensities changes. Recently, even quantitative measurements of ionization and recombination rates are reported by using the line-ratios and absolute emission intensities [9, 10].

While Balmer line spectroscopy has provided useful information, this diagnostic technique intrinsically measures line-integrated signals. When the plasma inside the emission volume along a line of sight cannot be treated as uniform, quantitative measurements are challenging. A closed-divertor plasma is one of those examples where spatial variations in plasma parameters are not negligible. However, accurate determination of parameters in this type of plasma is critical in understanding detachment in reactor-relevant conditions since it is widely accepted that the closed-divertor configuration facilitates detachment and will be the standard design for tokamak-based fusion reactors [1, 11].

In this paper, a new analysis technique for Balmer line spectroscopy that enables particle source and sink inference in a closed-divertor plasma is introduced. Instead of evaluating line-shapes or line ratios individually, the proposed analysis technique formulates a single inference problem by using a Bayesian framework. This approach allows for coherent addition of multiple Balmer lines in the analysis to further improve the measurements as more lines are resolved. In section 2, the relation between Balmer line emission and the recombination and ionization rates are discussed. The framework of Bayesian inference is explained by using a uniform plasma in section 3. Section 4 describes the details of the new analysis technique for a closed-divertor plasma. Also, the validation of this approach is provided by using divertor plasma simulations. In section 5, the new analysis method is applied to an L-mode plasma in ASDEX Upgrade (AUG). The discussion in section 4 and 5 is limited to the critical location in heat load mitigation, *i.e.*, the outer divertor. Finally, conclusions of this paper are given in section 6.

2. Relation between Balmer line emission and recombination and ionization rates

For Balmer lines, the local line emissivity coefficient is given by:

$$i_X(n_e,T_e,n_0)=n_en_i\mathrm{PEC}_X^{\mathrm{re}}(n_e,T_e)+n_en_0\mathrm{PEC}_X^{\mathrm{ex}}(n_e,T_e), \quad (1)$$

where $X=\varepsilon(n=7\rightarrow2)$, $\delta(n=6\rightarrow2)$, $\gamma(n=5\rightarrow2)$ and $\beta(n=4\rightarrow2)$. $\mathrm{PEC}_X^{\mathrm{re}}$ and $\mathrm{PEC}_X^{\mathrm{ex}}$ are photon emissivity coefficients for recombination emission and excitation emission, provided by ADAS [12], while n_e, n_i and n_0 are the electron density, ion density and neutral density, respectively. The first and second terms on the right hand side are recombination emission and excitation emission. In addition to these emission processes, molecular reactions can also contribute to the Balmer line spectrum [13]. The influence of the molecular reactions generally becomes larger for longer wavelengths [14]. Thus, $D_\alpha(n=3\rightarrow2)$ is excluded from the analysis in this paper. Lines with the upper state over $n=7$ are also excluded since measuring these lines is often difficult due to their weak emission intensities. While included in the analysis, care has to be taken when interpreting the discussion of $D_\beta(n=4\rightarrow2)$ since this line may also be affected by the molecular reactions under some circumstances. Equation (1) holds more rigorously for $D_\epsilon(n=7\rightarrow2)$, $D_\delta(n=6\rightarrow2)$ and $D_\gamma(n=5\rightarrow2)$[9, 10]. Another important effect, opacity, is also neglected in this analysis. Considering photon trapping may be critical especially for high-density divertors [14–16]. Including this effect remains future work. For the rest of the paper, it is assumed that the plasma is made solely of deuterium, *i.e.* $n_e=n_i$ as is done in Ref [9, 10]. This is a fair assumption for AUG since nitrogen ion concentration is typicallyless than a few percent in the outer divertor.

Figure 1 shows photon emissivity coefficients for each line. As the upper state increases from $n=4$ to 7 (β to ε), both $\mathrm{PEC}_X^{\mathrm{re}}$ and $\mathrm{PEC}_X^{\mathrm{ex}}$ decrease. It is important to note that the relative intensity between $\mathrm{PEC}_X^{\mathrm{re}}$ and $\mathrm{PEC}_X^{\mathrm{ex}}$ also varies. The crossing point between $\mathrm{PEC}_X^{\mathrm{re}}$ and $\mathrm{PEC}_X^{\mathrm{ex}}$ shifts to higher T_e as the energy of the upper state increases, indicating that D_β tends to be dominated by excitation emission while D_ϵ tends to have a dominant contribution from recombination emission. The dominant radiation process also depends strongly on T_e. As can be seen in figure 1, $\mathrm{PEC}_X^{\mathrm{ex}}$ drops sharply below 10 eV while $\mathrm{PEC}_X^{\mathrm{re}}$ increases as T_e decreases. The dependencies of PECs on n_e are moderate and the trends seen in figure 1 hold in the range of n_e relevant to divertor plasmas $\sim[10^{19}-10^{21}]$ m^{-3}. As equation (1) shows, PEC for recombination emission is multiplied by n_e^2 ($n_i=n_e$ is assumed) and PEC for excitation emission is multiplied by n_en_0. Thus, n_0 also contributes to the ratio of recombination to excitation emission.

The divertor plasma in a closed-divertor can have plasma parameters with significant spatial variations. Figure 2 shows the lines of sight in the outer divertor of AUG. To investigate how a line-integrated Balmer line emission intensity is related to the line-integrated ionization F_{io} and the line-integrated recombination rate F_{re}, a set of test data is generated from 17 different equilibria of AUG simulated by SOLPS [17]. 15 of them are H-mode [18] (drift included) and the rest are L-mode discharges (drift not included). For each equilibrum, test data corresponding to each line of sight shown in figure 2 is calculated. Typical parameter profiles along the red line of sight in figure 2 are shown in figure 3(a) (H-mode). In general, n_e and n_0 tend to be higher in the private flux region (PFR) than in the scrape-off layer (SOL) while T_e is typically higher in the SOL than in the PFR. The excitation and recombination emission

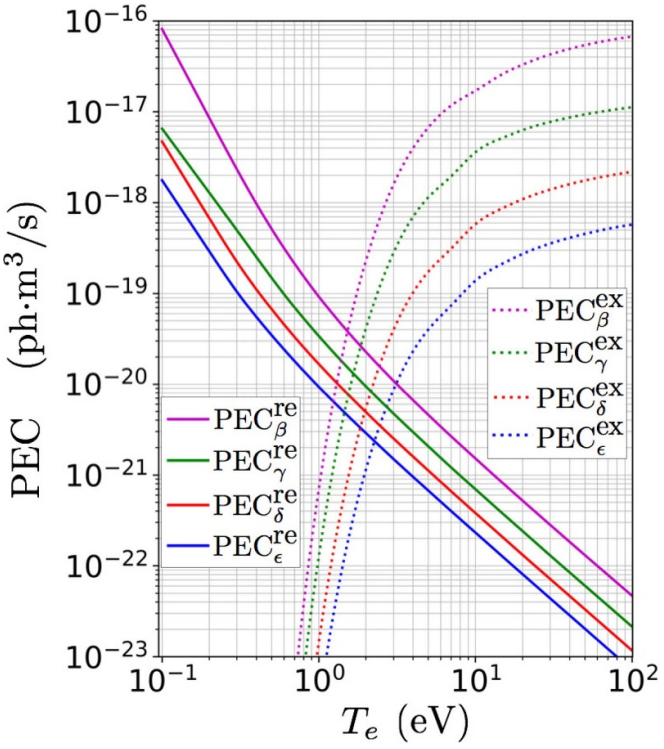

Figure 1. Recombination photon emissivity coefficients and excitation photon emissivity coefficients for $n_e = 1 \times 10^{20}$ m^{-3} from the ADAS data base [12]

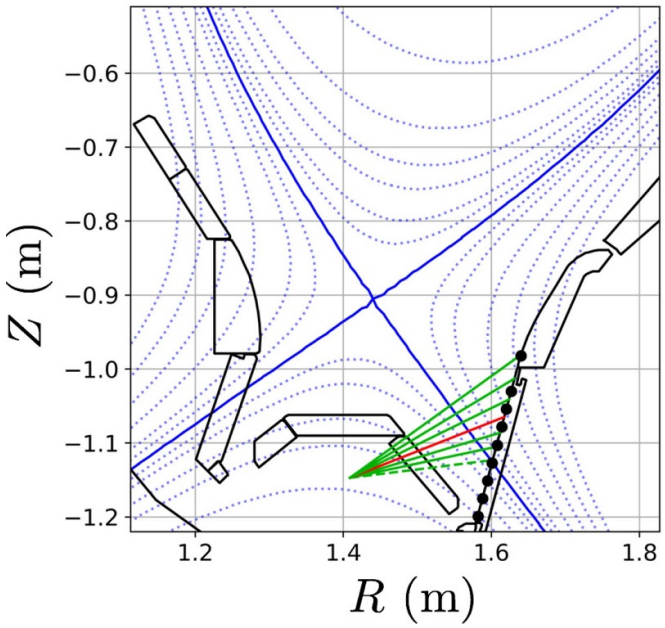

Figure 2. Lines of sight in the outer divertor of ASDEX Upgrade (Green and red lines). The lines of sight shown in solid lines are used for measurements discussed in section 5. The blue solid line is the separatrix and the blue dotted lines show flux surfaces. The black dots show the measurement points of Langmuir probes.

profiles for each Balmer line are shown in figures 3(b), (c), (e) and (f). The recombination emission mostly comes from the PFR whereas the SOL provides the majority of excitation emission. As the principle quantum number of the upper state increases, the line-integrated emission intensity is more dominated by the recombination emission than by the excitation emission as expected from figure 1

The spatial profiles of the ionization and recombination rates are shown in figure 3(d). Similar to the relation between the excitation and recombination emissions, the ionization rate is large in the SOL while the recombination rate peaks in the PFR. Figure 4(a) shows the relation between F_{re} and I_ϵ (the line-integrated emission intensity of D_ϵ), which tends to be dominated by recombination emission. The color of each point is a ratio of I_ϵ to I_δ (the line-integrated emission intensity of D_δ). This ratio is often used for characterizing which emission process dominates I_ϵ and I_δ[5]. The higher I_ϵ/I_δ, the more the recombination emission dominates compared to the excitation emission. The black dashed line is proportional to I_ϵ. Roughly linear relation between I_ϵ and F_{re} is seen except $I_\epsilon/I_\delta < 0.35$, where the excitation emission is non-negligible in I_ϵ. This scaling can be understood through figure 5(a) that shows an effective recombination coefficient ACD over $\mathrm{PEC}^{\mathrm{re}}_{\epsilon}$. This quantity represents a number of recombination events per photon due to the recombination emission in D_ϵ. The black dashed line in figure 4(a) is $F_{\mathrm{re}} = 1.81 \times 10^2 I_\epsilon$, indicating that about 181 recombination events happen for each photon in the D_ϵ emission. This proportional relation is also seen in Figs 3(b) and (d). The profile shape of the recombination emission in D_ϵ looks quite similar to that of the recombination rate. The combination of n_e and T_e corresponding to $F_{\mathrm{re}} = 1.81 \times 10^2 I_\epsilon$ is shown by the thick red line in figure 5(a). The dependency of ACD/$\mathrm{PEC}^{\mathrm{re}}_{\epsilon}$ on T_e and n_e is moderate for $T_e > 1$ eV. While $\mathrm{PEC}^{\mathrm{re}}_{\epsilon}$ increases as T_e decreases for $T_e < 1$ eV, I_ϵ is rarely dominated by the emission coming from regions with $T_e < 1$ eV since n_e there is significantly lower than near the separatrix due to frequent recombination. Therefore, F_{re} roughly scales linearly with I_ϵ for $I_\epsilon/I_\delta > 0.35$.

Contrary to I_ϵ, I_β tends to be dominated by excitation emission. Figure 4(b) shows the relation between F_{io} and I_β. While a correlation can be seen, the data points scatter more widely compared with figure 4(a). In some cases, F_{io} differs by a factor of ~ 2 for the same I_β. The ratio of an effective ionization coefficient SCD to $\mathrm{PEC}^{\mathrm{ex}}_{\beta}$ (the number of ionization events per photon due to excitation emission in D_β) is shown in figure 5(b). SCD/$\mathrm{PEC}^{\mathrm{ex}}_{\beta}$ depends strongly on n_e. Below $T_e < 10$ eV, the T_e dependence on SCD/$\mathrm{PEC}^{\mathrm{ex}}_{\beta}$ is also strong, indicating that proportionality between I_β and F_{io} is not expected. While educated guesses may be made by using empirical formulae that relate I_β to F_{io} from the SOLPS simulation results, the focus of this paper is to infer ionization and recombination rates based on a physics model, which will be discussed in the following sections.

3. D_ϵ and D_δ spectroscopy for a uniform plasma slab using Bayesian inference

The diagnostic techniques discussed in the rest of the paper employ Bayesian inference to extract maximum available

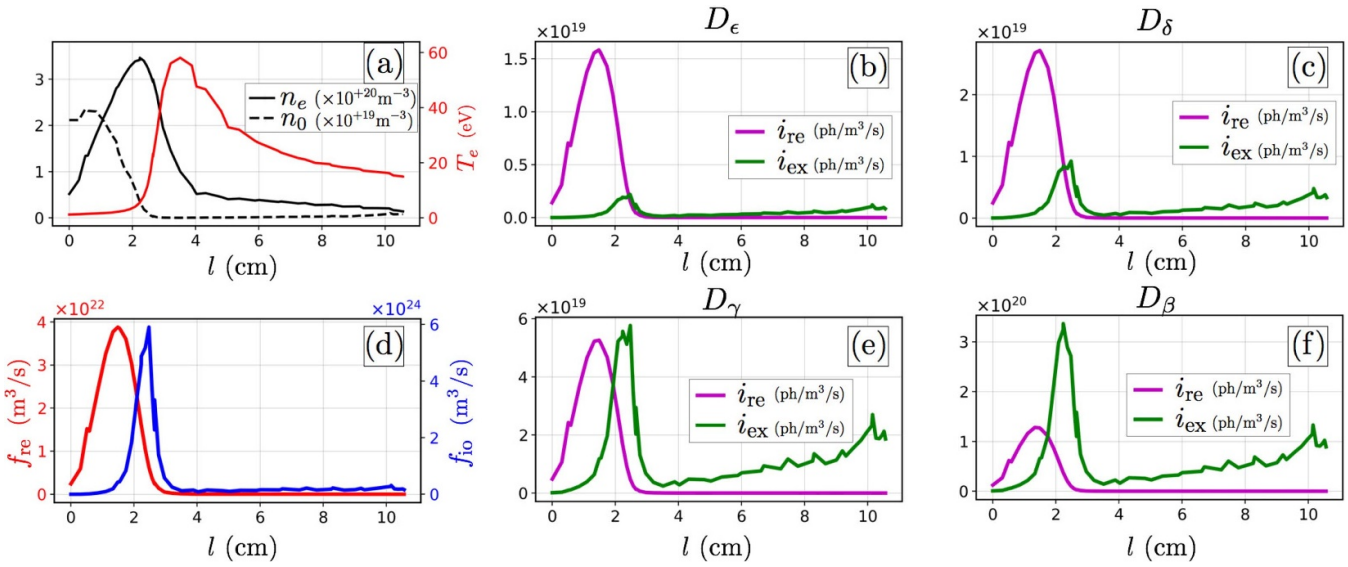

Figure 3. (a) Typical plasma parameter profiles (n_e, n_0 and T_e) along the line of sight shown in red in figure 2. Profiles of recombination emission i_{re} and excitation emission i_{ex} for each Balmer line are shown in (b), (c), (e) and (f). (d) Profiles of the recombination rate f_{re} and ionization rate f_{io}. The x axis ranges from the PFR to the SOL. The separatrix is near 3 cm.

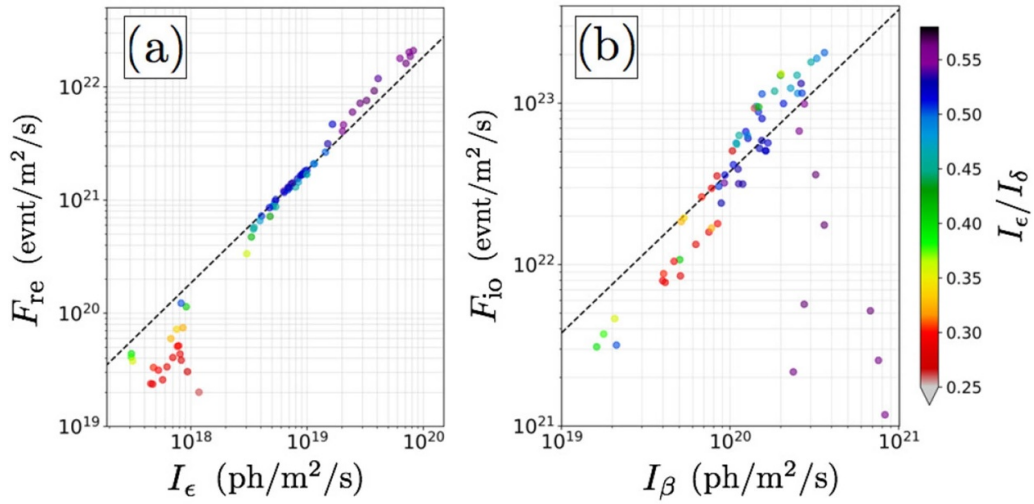

Figure 4. Relations between the line-integrated D_ϵ emission intensity I_ϵ and line-integrated recombination rate F_{re} (a) and between the line-integrated D_β emission intensitiy I_β and line-integrated ionization rate F_{io} (b). The black dotted lines show the proportional relations.

information from limited data. In this section, basic framework of Bayesian inference for Balmer line spectroscopy is described before the technique is applied to the plasma in a closed-divertor.

Since Balmer line emission depends on multiple plasma parameters in a complex fashion, available measurements often fail to provide sufficient information to uniquely determine each plasma parameter, *i.e.*, the problem is underdetermined. However, within the framework of Bayesian inference, possible ranges of unknown parameters can be infered. For demonstration purposes, measurements of a uniform plasma slab using two Balmer lines D_ϵ and D_δ are discussed. As mentioned in the introduction, when $n_e \gtrsim 4 \times 10^{19}$ m^{-3}, n_e can be reliably measured by fitting a Stark-broadened D_ϵ line. Due to the proximity of D_δ to D_ϵ in wavelength, these two Balmer lines are often measured simultaneously with high wavelength resolution using a single spectrometer [5, 9, 10]. For a uniform plasma, the measured emission intensity of D_ϵ and D_δ are:

$$I_\epsilon = \delta l[n_e^2 \mathrm{PEC}_\epsilon^{\mathrm{re}}(n_e, T_e) + n_e n_0 \mathrm{PEC}_\epsilon^{\mathrm{ex}}(n_e, T_e)], \qquad (2)$$

$$I_\delta = \delta l[n_e^2 \mathrm{PEC}_\delta^{\mathrm{re}}(n_e, T_e) + n_e n_0 \mathrm{PEC}_\delta^{\mathrm{ex}}(n_e, T_e)], \qquad (3)$$

where δl is the length of the emission volume along a line of sight, which is unknown this case. Note that the plasma is assumed to be made of pure deuterium, *i.e.*, $n_i = n_e$. In Balmer line spectroscopy for divertor plasmas, the ratio I_ϵ / I_δ is often

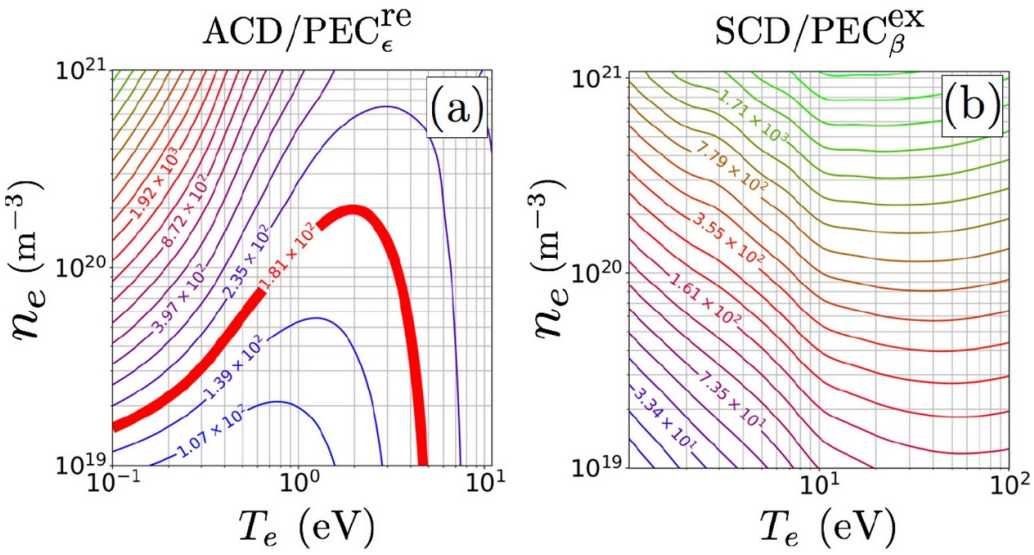

Figure 5. (a) Ratio of the effective recombination rate (ACD) to the recombination photon emissivity coefficient for D_ϵ (PEC$_\epsilon^{\rm re}$). (b) Ratio of the effective ionization rate (SCD) to the excitation photon emissivity coefficient for D_β (PEC$_\beta^{\rm ex}$). The level of contour lines increases by 30% between adjacent lines. ACD and SCD are provided by ADAS [12].

evaluated [5, 9, 10]. While I_ϵ/I_δ is independent of δl, there are still two undetermined plasma parameters, n_0 and T_e. Therefore, neither of them can be determined without assuming the other. Figure 6 shows the ratios of PEC$_\epsilon^{\rm ex,re}$ to PEC$_\delta^{\rm ex,re}$. Those plots imply that I_ϵ/I_δ is low when excitation emission is dominant (or high when recombination emission is dominant).

From the line ratio I_ϵ/I_δ, possible combinations of n_0 and T_e are determined for a given n_e. While they produce the same I_ϵ/I_δ ratio, the absolute light intensities vary. The possible range of δl can be estimated from the viewing geometry and knowledge about the plasma, *e.g.*, δl is shorter than a line of sight. Therefore, the ranges of n_0 and T_e can be constrained by calculating δl corresponding to each combination of n_0 and T_e. To investigate the relation between δl, n_0 and T_e, three cases with different I_ϵ/I_δ ratios given in table. 1 are considered. In the Bayesian framework, a forward model calculates synthetic data in a parameter space defined by a prior. Since a likelihood evaluates how much the synthetic data is close to the experimentally measured data, the absolute intensities of D_ϵ and D_δ are automatically taken into account as well as the line ratio. The probability distributions of the parameters given that data $\boldsymbol{D}$ is observed are given by Bayes' Rule [19]:

$$p(\boldsymbol{\theta}|\boldsymbol{D},I) = \frac{p(\boldsymbol{D}|\boldsymbol{\theta},I)p(\boldsymbol{\theta}|I)}{p(\boldsymbol{D}|I)}, \tag{4}$$

where I is prior information and $\boldsymbol{\theta}$ is the parameters in the forward model. In this case, $\boldsymbol{D} = [I_\epsilon, I_\delta]$ and $\boldsymbol{\theta} = [\delta l, n_0, T_e]$. In this analysis, each element of $\boldsymbol{\theta}$ is allowed to vary many orders of magnitude. To avoid biasing distribution toward higher orders of magnitude [19, 20], the following prior distributions are used:

$$\begin{aligned} T_e &= 10^a \ \text{eV}, \quad a \in [-1.0, 2.3], \\ n_0 &= 10^b \ \text{m}^{-3}, \quad b \in [15.0, 24.0], \\ \delta l &= 10^c \ \text{m}, \quad c \in [-4.0, 2.0], \end{aligned} \tag{5}$$

where a, b and c have uniform distributions within the specified ranges. The likelihood is given by:

$$p([I_\epsilon, I_\delta]|[T_e, n_0, \delta l], I) = \prod_{X=\epsilon,\delta} \frac{1}{\sqrt{2\pi\sigma_{I_X}^2}} \exp\left(-\frac{(I_X - I_X^{\rm FWM})^2}{2\sigma_{I_X}^2} \right), \tag{6}$$

where $I_X^{\rm FWM}$ is the forward-modeled Balmer line intensity, which is calculated by inserting T_e, n_0 and δl into equations (2) and (3). Note that n_e is independently measured and not an element of $\boldsymbol{\theta}$. The measurements of I_ϵ and I_δ are assumed to have a relative uncertainty of 3%, *i.g.*, $\sigma_{I_\epsilon, I_\delta} = 0.03 \times I_{\epsilon,\delta}$. The evidence $p(\boldsymbol{D}|I)$ is neglected since the absolute probability is not of interest. Due to the low dimensionality, a brute force algorithm is employed and an unnormalized posterior is calculated for each point in the three dimensional space $[T_e, n_0, \delta l]$. Figures 7, 8 and 9 show the posterior distributions and the marginalized distributions in terms of one of the thee parameters for each case: I_ϵ/I_δ =0.46, 0.32 and 0.25.

The contour line 0.46 corresponding to Case 1 is indicated in figure 6(a). $I_\epsilon/I_\delta = 0.46$ can also be realized by mixing recombination emission with PEC$_\epsilon^{\rm re}$/PEC$_\delta^{\rm re} > 0.46$ and excitation emission with PEC$_\epsilon^{\rm ex}$/PEC$_\delta^{\rm ex} < 0.46$. Note that PEC$_{\epsilon,\delta}^{\rm re} \gg$ PEC$_{\epsilon,\delta}^{\rm ex}$ below 1 eV as shown in figure 1. Therefore, excitation emission is negligible with respect to recombination emission for $T_e < 1$ eV unless n_0 is greater than n_e by many orders of magnitude. Below 1 eV, a band of high probability range is seen along the n_0 axis in figures 7(a), (b) and (c). This structure corresponds to the parameter range that reproduces the observed I_ϵ and I_δ with recombination emission only. Since excitation emission does not contribute to the total light intensity, the probability distribution of n_0 is flat, *i.e.*, n_0 is undetermined. The other high probability structure that depends on

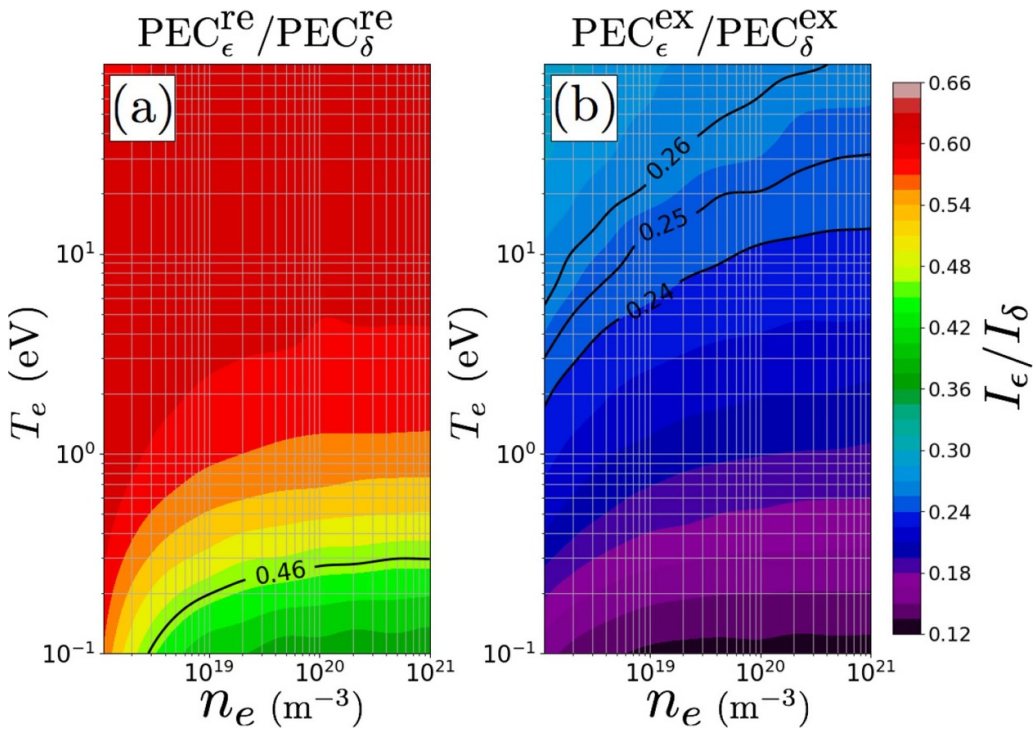

Figure 6. Ratios of $\mathrm{PEC}_\epsilon^{\mathrm{re}}$ to $\mathrm{PEC}_\delta^{\mathrm{re}}$ (a) and $\mathrm{PEC}_\epsilon^{\mathrm{ex}}$ to $\mathrm{PEC}_\delta^{\mathrm{ex}}$ (b) as a function of n_e and T_e.

Table 1. Emission intensities of D_ϵ and D_δ and their ratio for each case.

	n_e	I_ϵ	I_δ	I_ϵ/I_δ
Case 1	8.4×10^{19} m^{-3}	6.9×10^{18} ph/(m^2·s)	1.5×10^{19} ph/(m^2·s)	0.46
Case 2	8.4×10^{19} m^{-3}	7.4×10^{18} ph/(m^2·s)	2.3×10^{19} ph/(m^2·s)	0.32
Case 3	8.4×10^{19} m^{-3}	2.8×10^{18} ph/(m^2·s)	1.1×10^{19} ph/(m^2·s)	0.25

all T_e, n_0 and δl reproduces I_ϵ and I_δ with both recombination and excitation emissions. While there are two ways of achieving the ratio I_ϵ/I_δ of 0.46, the required size of the plasma δl that reproduces the observed absolute light intensities is different. If it is known that δl is less than a few cm, the observed ratio can be realized by only recombination. In this case, there are only two unknowns, T_e and n_e, for two equations (2) and (3). Therefore, the problem is not underdetermined and T_e and n_e are uniquely determined. In this case, $T_e\approx$ 0.3 eV where the vertical band peaks in figure 7 b and $\delta l\approx 8\times10^{-3}$m where the horizontal band peaks in figure 7(c). It is not possible to constrain the range of n_0 more than what the prior does. When $\delta l > 0.8\times10^{-2}$ m, both recombination and ionization contribute to the total light intensity. If one of T_e, n_0 and δl is given, the other two that reproduce I_ϵ and I_δ are determined. It is important to note that figure 7(b) is dependent only on the ratio I_ϵ/I_δ and independent of the absolute light intensities. When the absolute emission intensities vary with I_ϵ/I_δ fixed, the probability distributions shown in figure 7 move along the δl direction, but the shapes of them do not change. This is also true for Case 2 and Case 3.

In Case 2 shown figure 8, the I_ϵ/I_δ ratio is 0.32. This I_ϵ/I_δ cannot be realized by only recombination as can be seen from figure 6. Therefore, the band of high probability range along the n_0 direction observed in figure 7 is absent in figure 8. While the exact values of I_ϵ and I_δ can never be reproduced without ionization emission, the likelihood given by equation (6) becomes large near $[T_e, \delta l] = [0.1\,\mathrm{eV}, 10^{-3}\,\mathrm{m}]$. This effect accumulates when marginalized in terms of n_0 and leads to a spot of high probability near the y aixs in figure 8(d). The absence of high probability region below $\delta l = 4\times10^{-2}$ m and $T_e = 8\times10^{-1}$ eV is due to the prior of n_0.

In Case 3 ($I_\epsilon/I_\delta = 0.25$), excitation emission dominates I_ϵ and I_δ. The high probability range traces out a surface instead of a curve in figure 9(a). In principle, when recombination emission is negligible, T_e is uniquely determined by the I_ϵ/I_δ ratio based on equations (2) and (3). However, it is difficult to infer T_e from figure 9(b) or (d). When the excitation emission is negligible, T_e also uniquely determines the absolute intensities of I_ϵ and I_δ as well as the I_ϵ/I_δ ratio for given n_e and δl. In contrast, the intensity of excitation emission depends also on n_0, which is not known. Therefore, the absolute intensities do not provide a strong constraint. The assumed 3% uncertainty in the I_ϵ and I_δ measurements translates to about the uncertainty of 0.1 in the I_ϵ/I_δ ratio. The T_e range corresponding to I_ϵ/I_δ =0.24 to 0.26 shown in figure 6(b) is rather

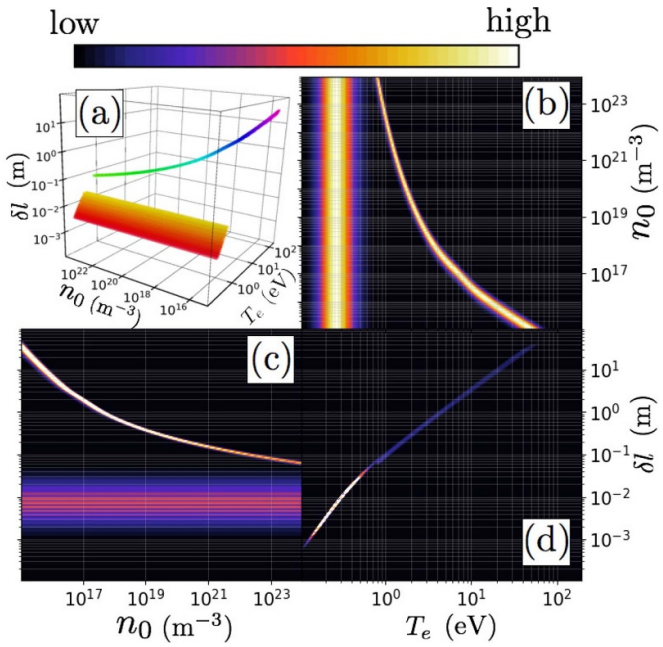

Figure 7. Case 1 for $I_\epsilon/I_\delta = 0.46$. A posterior distribution (a) and marginalized posterior distributions (b), (c) and (d). A volume where $2\pi\sigma_{I_\epsilon}\sigma_{I_\delta}p(\boldsymbol{D}|\boldsymbol{\theta},I) > 1/e$ is shown in (a),.

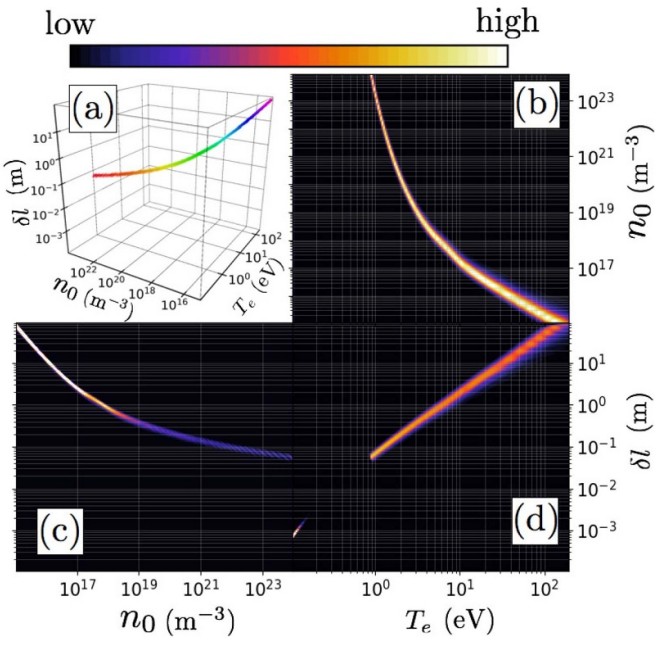

Figure 8. Case 2 for $I_\epsilon/I_\delta = 0.32$. A posterior distribution (a) and marginalized posterior distributions (b), (c) and (d). A volume where $2\pi\sigma_{I_\epsilon}\sigma_{I_\delta}p(\boldsymbol{D}|\boldsymbol{\theta},I) > 1/e$ is shown in (a),.

wide. Measuring T_e is not practical when excitation emission dominates the total light intensities unless I_ϵ and I_δ can be measured with precision much better than what is assumed in Case 3. Uncertainties in photon emissivity coefficients, which are neglected in this paper, are also expected to affect the measurement in this case. Figure 1 shows that the dependence of $\mathrm{PEC}^{\mathrm{ex}}_{\epsilon,\delta}$ on T_e becomes weak as T_e increases. Thus, the total light intensity depends mostly on the product of δl and n_0 for high T_e, leading to the linear trend between δl and n_0 in figure 9(c).

In this section, only D_ϵ and D_δ are considered. When three lines are resolved, T_e, n_0 and δl are uniquely determined. When more than three lines are measured, the problem becomes over-constrained. However, equation (6) can be extended to arbitrary numbers of Balmer lines by multiplying the likelihood for each line and the probability distributions of T_e, n_0 and δl are obtained by utilizing all available information in a coherent fashion. This modular concept is one of the advantages of the Bayesian framework [21].

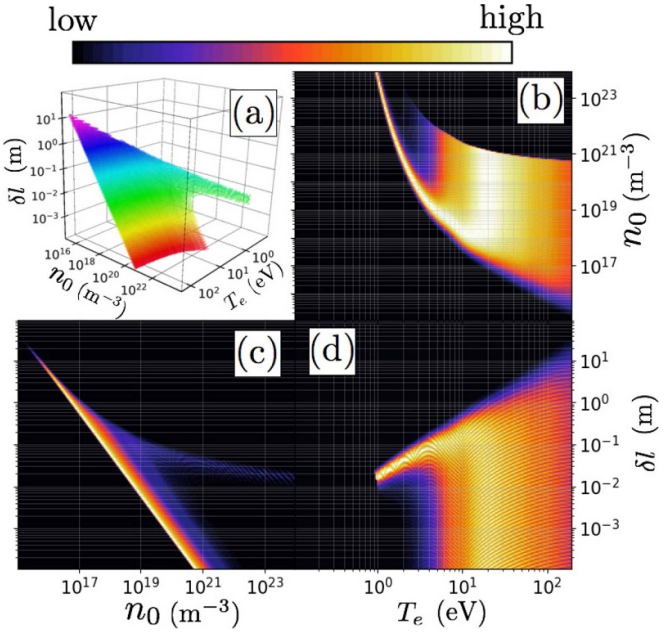

Figure 9. Case 3 for $I_\epsilon/I_\delta = 0.25$. A posterior distribution (a) and marginalized posterior distributions (b), (c) and (d). A volume where $2\pi\sigma_{I_\epsilon}\sigma_{I_\delta}p(\boldsymbol{D}|\boldsymbol{\theta},I) > 1/e$ is shown in (a),.

4. Inferring line-integrated recombination and ionization rates in a closed-divertor using a simplified profile model

In the previous section, the methodology for inferring the plasma parameters of a uniform plasma is discussed. As figure 3(a) shows, spatial variations of plasma parameters are not negligible in a closed-divertor plasma and the discussion for a uniform plasma slab is not necessarily applicable. Inferring local plasma parameters is challenging by only using line-integrated measurements through the lines of sight shown in figure 2. However, as can be seen in figure 4, line-integrated recombination and ionization rates are correlated to measurable quantities such as I_ϵ, or I_β, suggesting that line-integrated plasma parameters can still be inferred. In this section, the analysis technique for line-integrated recombination and ionization rates (F_{re} and F_{io}) in a closed-divertor geometry is discussed.

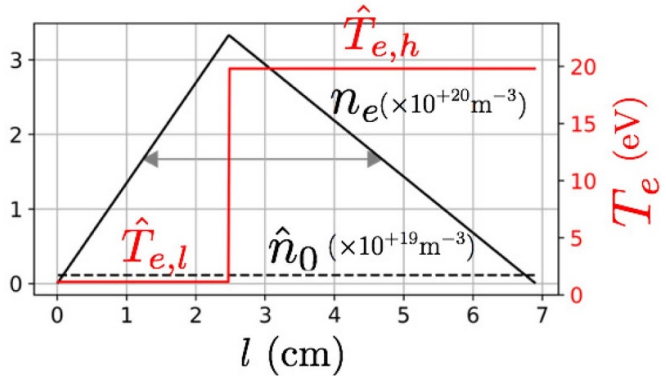

Figure 10. Profiles of n_e, T_e and n_0 in a simplified profile model (SPM). The separatrix is at $l = \hat{\alpha}\hat{l}$.

The plasma parameter profiles shown in figure 3 (a) represent general features of outer-divertor plasmas in AUG. The peak of n_e is near the separatrix. There are typically large differences in T_e and n_0 between the PFR and the SOL. In general, complex forward models with many parameters lead to wide probability distributions of individual parameters when marginalized. However, if a forward model is too simple and fails to capture important features of true physical processes, significant mismatches between the true values and inferred values occur. Therefore, a forward model for the F_{re} and F_{io} inference needs to have sufficient flexibilities to match real plasma parameter profiles while keeping the number of parameters in the model to a minimum. A simplified profile model (SPM) shown in figure 10 is employed for the forward model in this analysis. SPM has six parameters: $\boldsymbol{\theta} = [\hat{l}, \hat{\alpha}, \hat{n}_e, \hat{T}_{e,l}, \hat{T}_{e,h}, \hat{n}_0]$. The FWHM of the n_e profile is $\hat{l}$. The triangular shape of n_e profile can be asymmetric. The peak position of n_e is specified by a parameter $\alpha \in [0, 2]$. The n_e value at the half-maximum is $\hat{n}_e$. The T_e profile has a step at the peak of n_e. The lower value corresponding to the PFR is $\hat{T}_{e,l}$ and the higher value corresponding to the SOL is $\hat{T}_{e,h}$. Even though there is typically a large difference in n_0 between the PFR and the SOL, the n_0 profile is uniform in SPM. Practically, $\hat{n}_0$ represents n_0 in the SOL. The emission profiles shown in figures 3(b), (c), (e) and (f) indicate that the majority of excitation emission occurs in the SOL. Since $\mathrm{PEC}^{\mathrm{ex}}_X$ decreases by many orders of magnitude as T_e drops from 10 to 1 eV (shown in figure 1), excitation emission in the PFR is small despite the higher n_0. In addition, ionization, which also depends on n_0, occurs mostly in the SOL. Therefore, the calculation of synthetic data and the inference of F_{io} are relatively insensitive to the underestimation of n_0 in the PFR.

In the previous section, the data are $\boldsymbol{D} = [I_\epsilon, I_\delta]$ (intensities of D_ϵ and D_δ lines). However, Balmer line spectroscopy originally measures intensities of wavelength channels and n_e is inferred by the Stark-broadened line shape. Thus, $\boldsymbol{D}$ should be the intensities of wavelength channels. The synthetic data based on SPM is given by:

$$I^{\mathrm{SPM}}_{X,\lambda_X} = \int d\lambda H_{\lambda_X}(\lambda) \int_0^{2\hat{l}} dl \cdot i_X(\boldsymbol{\theta}) L_X(\lambda, \boldsymbol{\theta}), \tag{7}$$

where $X = \varepsilon, \delta, \gamma$, and β. The line emissivity coefficient i_X is already defined by equation (1). The normalized line shape of a Balmer line X is given by L_X and H_{λ_X} is an instrument broadening function. There are many line shape models with different complexities for Balmer lines [4, 6, 7]. This analysis uses a relatively simple model provided by Ref [7]:

$$L_X(\lambda, n_e, T_e) \propto \frac{1}{(\lambda - \lambda_{0,X})^{5/2} + (c_X \frac{n_e^{a_X}}{T_e^{b_X}})^{5/2}}, \tag{8}$$

where $\lambda_{0,X}$ is the central wavelength of a Balmer line X. Each Balmer line has different values for coefficients, a_X, b_X and c_X. Many processes cause broadening. Here, only Stark-broadening, from which n_e is measured and the instrument function of a spectrometer are considered. These two are typically dominant for D_ϵ and D_δ measurements of conduction-limited divertor plasmas at AUG. The instrument function of a wavelength channel λ_X is:

$$H_{\lambda_X} = \frac{1}{\sqrt{2\pi\sigma_X^2}} \exp\left(- \frac{(\lambda - \lambda_X)^2}{2\sigma_X^2} \right), \tag{9}$$

where σ_X is the wavelength resolution of a spectrometer, $\sigma_X \approx$ 35 pm (σ_X is slightly different for each λ_X). For D_γ and D_β lines, the instrument broadening is dominant and practically only absolute intensities provide constraints. Local emission as a function of wavelength λ is integrated along the line of sight l. Then, instrumental effects are taken into account by integrating in terms of λ.

A probability distribution of $\boldsymbol{\theta}$ given the experimental measurements is calculated, again, by using the Bayes' theorem. Assuming that errors in the measurements follow a Gaussian distribution, the likelihood is given by:

$$p(\boldsymbol{D}|\theta, I) = \prod_X \prod_{\lambda_X} \frac{1}{\sqrt{2\pi\sigma_{\lambda_X}^2}} \exp\left(- \frac{(I_{X,\lambda_X} - I^{\mathrm{SPM}}_{X,\lambda_X})^2}{2\sigma_{\lambda_X}^2} \right), \tag{10}$$

where I_{X,λ_X} is the experimentally measured intensity of the wavelength channel λ_X and σ_{λ_X} is the uncertainty of I_{X,λ_X}. The product over λ_X includes wavelength channels near a Balmer line X. Once a probability distribution is calculated in the $\boldsymbol{\theta}$ space, the distribution can be mapped onto probability distributions of F_{re} and F_{io} using an effective recombination rate ACD and an effective ionization rate SCD discussed in section 2 The validity of SPM is tested by using the same set of SOLPS simulation data used for figure 4. The uncertainties σ_{λ_X} are set to be 3% of the maximum intensity of the line X, *i.e.*, $\sigma_{\lambda_X} = 0.03 \times \max(I_{X,\lambda_X})$. While σ_{λ_X} depends on the diagnostic setup, this analysis is underdetermined. Thus, as is discussed in section 3, some degree of uncertainties are expected to entail even when σ_{λ_X} is infinitesimally small. In the real measurements discussed in the next section,

$$\sigma_{\lambda_X} = \sqrt{\sigma^2{}_{\lambda_X,\mathrm{ph}} + \sigma^2{}_{\lambda_X,\mathrm{int}}}, \tag{11}$$

where $\sigma^2{}_{\lambda_X,\mathrm{ph}}$ is the photon counting noise (Poisson noise) [22] and $\sigma^2{}_{\lambda_X,\mathrm{int}}$ is the intrinsic noise in the data acquisition

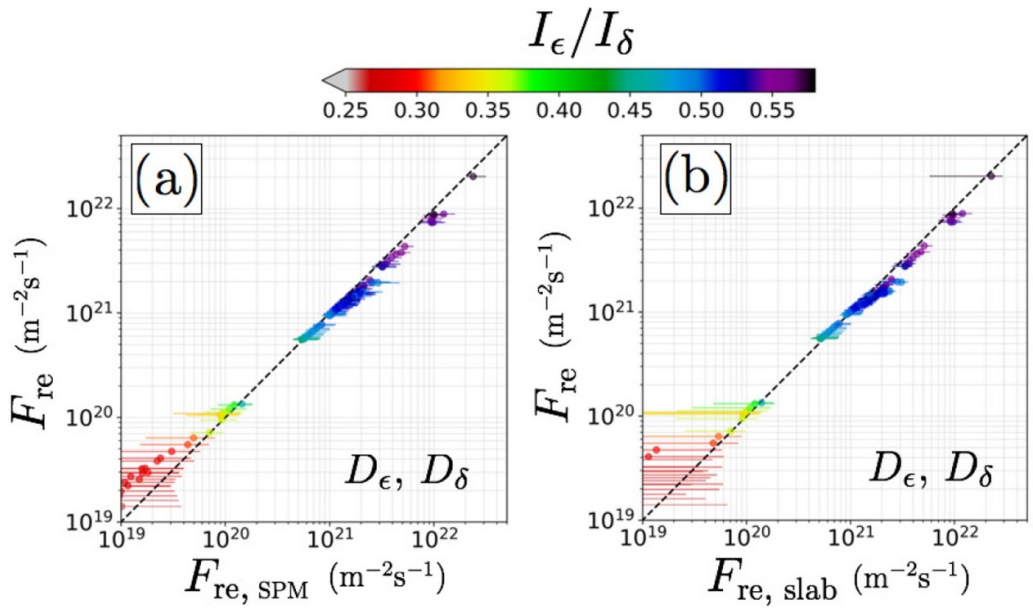

Figure 11. Comparison between line-integrated recombination rates calculated by the Bayesian inference and true values. (a)Line integrated ionization rates inferred by SPM when D_ϵ and D_δ are measured. (b)Line integrated recombination rates inferred by the uniform slab model when D_ϵ and D_δ are measured. The y axes are the true line-integrated recombination rates calculated directly from the SOLPS simulations. The color represents the emission intensity ratio of D_ϵ to D_δ. The data points are the 50th percentiles of the probability distributions of recombination rates. The errors show the range between the 16th and the 84th percentiles.

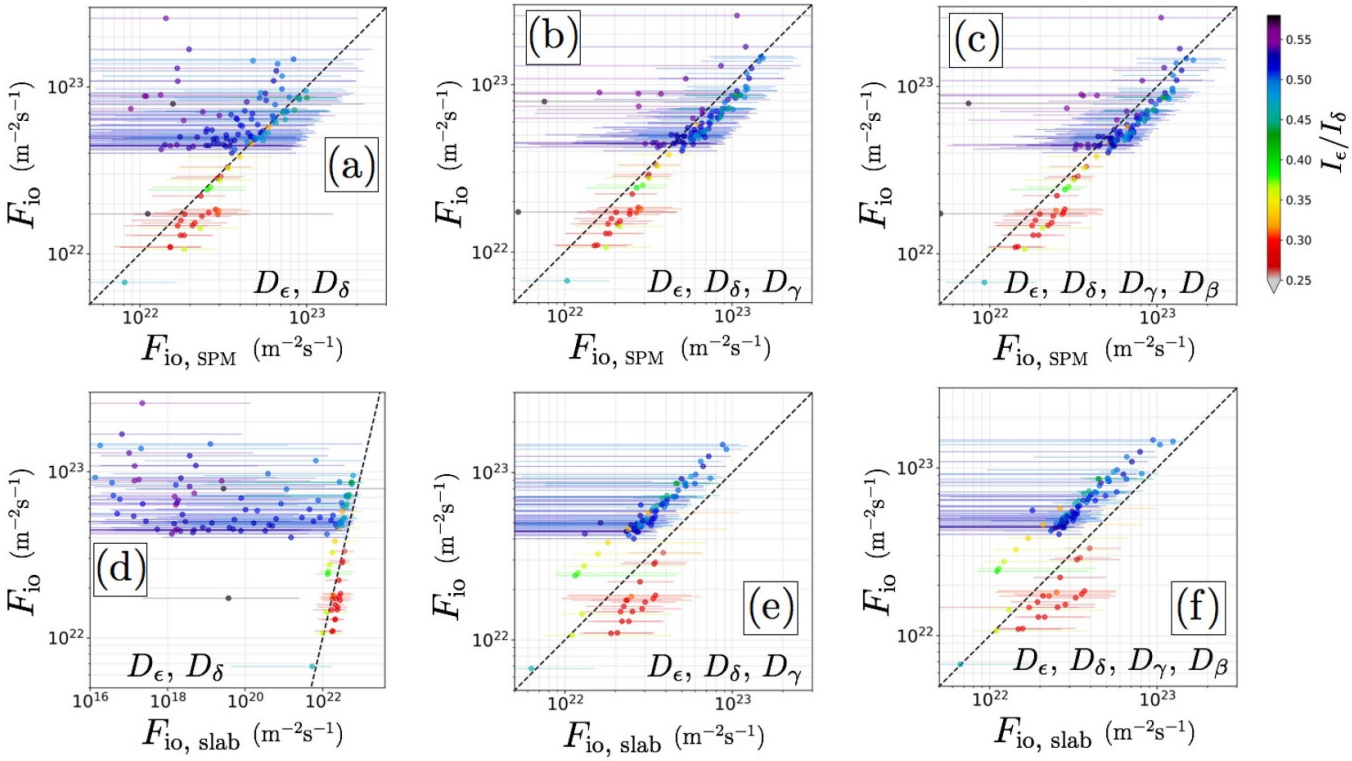

Figure 12. Comparison between line-integrated ionization rates calculated by the Bayesian inference and true values. Line integrated ionization rates inferred by SPM: (a) D_ϵ and D_δ measurement, (b) D_ϵ, D_δ and D_γ measurement and (c) D_ϵ, D_δ, D_γ and D_β measurement. Line integrated ionization rates inferred by the uniform slab model: (d) D_ϵ and D_δ measurement, (e) D_ϵ, D_δ and D_γ measurement and (f) D_ϵ, D_δ, D_γ and D_β measurement. The y axes are the true line-integrated ionization rates calculated directly from the SOLPS simulations. The color represents the emission intensity ratio of D_ϵ to D_δ. The data points are the 50th percentiles of the probability distributions of ionization rates. The errors show the range between the 16th and the 84th percentiles.

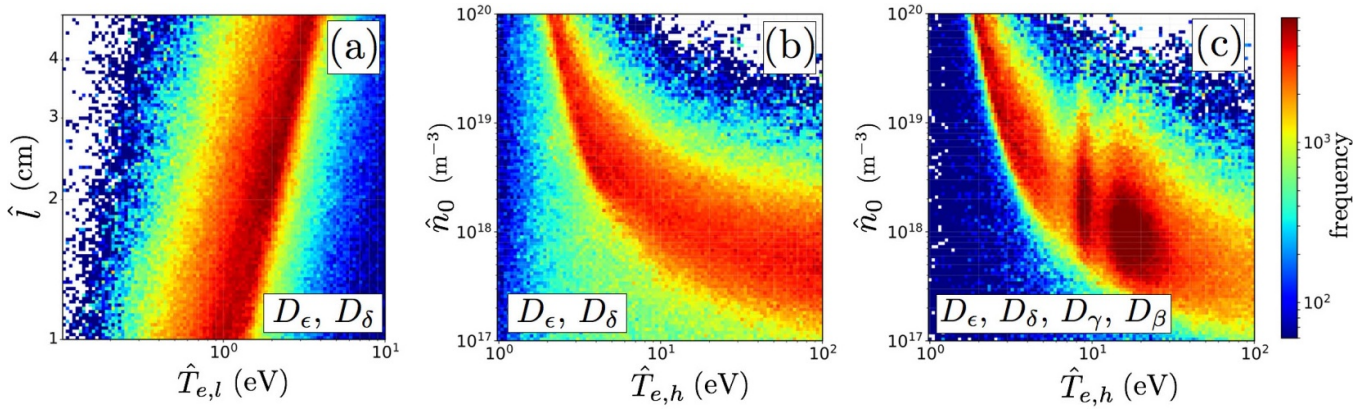

Figure 13. (a) Correlation between $\hat{T}_{e,l}$ and $\hat{l}$ when D_ϵ and D_δ are measured. (b) Correlation between $\hat{T}_{e,h}$ and $\hat{n}_0$ when D_ϵ and D_δ are measured. (c) Correlation between $\hat{T}_{e,l}$ and $\hat{l}$ when D_ϵ, D_δ, D_γ and D_β are measured. The input data for the Balmer line measurements are generated from the plasma parameter profiles shown in figure 3

system. The uncertainties in absolute intensity calibration is absorbed into the prior of $\hat{l}$. See appendix A for the details. Priors are given by:

$$\begin{aligned}
\hat{l} &= 10^A \text{ cm}, \quad A \in [\log_{10} 1, \log_{10} 5], \\
\hat{\alpha} &\in [0, 2], \\
\hat{n}_e &\in [1 \times 10^{19} \text{m}^{-3}, 9 \times 10^{20} \text{m}^{-3}], \\
\hat{T}_{e,l} &= 10^B \text{ eV}, \quad B \in [\log_{10} 0.1, \log_{10} 100], \\
\hat{T}_{e,h} &= 10^C \text{ eV}, \quad C \in [\log_{10} 0.1, \log_{10} 100], \\
\hat{n}_0 &= 10^D \text{ m}^{-3}, \quad D \in [17, 20],
\end{aligned} \tag{12}$$

where A, B, C, D, $\hat{\alpha}$ and $\hat{n}_e$ have uniform distributions within the specified ranges. A linear prior is chosen for $\hat{n}_e$ since, due to the strong constraint given by the Stark broadening of D_ϵ, the marginalized probability distribution for $\hat{n}_e$ is strongly peaked and biasing toward higher magnitudes is not observed. In order to properly sample a non-monomodal posterior probability distribution, the parallel tempering algorithm [23] in the emcee library is employed [24]. The integral over l is calculated by using ten steps along the line of sight. Five of them are in the PFR, the other five in the SOL. The difference in the inferred values is marginal when finer steps are used. The inferred line integrated recombination rate $F_{\text{re,SPM}}$ and line integrated ionization rate $F_{\text{io,SPM}}$ are compared with true values directly calculated from the SOLPS simulation profiles. Figures. 11(a) and 12(b) show the relation between the inferred values and true values when D_ϵ and D_δ are measured. While F_{re} is inferred with reasonable precision, the F_{io} inference suffers from large uncertainties especially when $I_\epsilon/I_\delta > 0.45$. The result of the F_{io} inference when D_γ is included in the measurement is shown in figure 12(b). The uncertainties are significantly reduced compared with figure 12(a). Further improvement is seen in figure 12(c) which shows the results when D_ϵ, D_δ, D_γ and D_β are measured. The reason for this improvement can be seen in the correlations between the parameters in SPM. Figure 13 shows marginalized probability distributions corresponding to the plasma parameter profiles shown in figure 3 ($I_\epsilon/I_\delta = 0.47$). A strong correlation between $\hat{T}_{e,l}$ and $\hat{l}$ is seen in figure 13(a). For the data points with $I_\epsilon/I_\delta > 0.45$, recombination emission dominates the D_ϵ and D_δ emission. As T_e increases, $\text{PEC}^{\text{re}}_{\epsilon,\delta}$ decreases. Therefore, a larger emission volume is required to keep the emission intensities constant for lower $\hat{T}_{e,l}$. On the other hand, the correlation between $\hat{T}_{e,h}$ and $\hat{l}$ is weak (not shown). Excitation emission provides 'fine adjustment' to realize the observed line ratio. The strong correlations between $\hat{T}_{e,h}$ and $\hat{n}_0$ shown in figures 13(b) and (c) are expected since excitation emission depends on both $\hat{T}_{e,h}$ and $\hat{n}_0$. However, the probability distribution in figure 13(b) has relatively high amplitude below the high amplitude band. In this range, excitation emission is negligible in I_ϵ and I_δ and the observed data can be reproduced with only recombination emission. Since the information on n_0, which the ionization rate is proportional to, is contained only in excitation emission, 'recombination only solutions' lead to large uncertainties in the F_{io} inference. In contrast, figure 13(c) shows much lower amplitude below the high amplitude band. Due to high sensitivities of D_γ and D_β to excitation emission, recombination emission alone cannot reproduce the observed D_γ and D_β emission. The relation between the size of error bars and the I_ϵ/I_δ ratio can be understood through the contribution of the excitation emission. In figure 12(a), the data points with high I_ϵ/I_δ, which are dominated by recombination emission, tend to have larger error bars. When $I_\epsilon/I_\delta > 0.54$, excitation emission becomes negligible even in the D_γ and D_β emission, leading to large error bars shown in Fig2. 12(b) and (c). For $I_\epsilon/I_\delta < 0.54$, the 50th percentile of $F_{\text{io,SPM}}$ systematically overestimates F_{io}. It is thought to originate from the triangular shape of the n_e profile in SPM. SPM approximates the n_e profiles in the SOL, which looks more like exponential in figure 3, by using a linear function. Figure 5(b) shows that $\text{SCD/PEC}^{\text{ex}}_{\beta}$ is relatively insensitive to T_e above 10 eV, which is a typical T_e in the SOL. However, $\text{SCD/PEC}^{\text{ex}}_{\beta}$ depends strongly on n_e, indicating that assigning proper n_e is more important then T_e for inferring F_{io}. Due to the limited flexibility, SPM tends to reproduce the excitation emission by using higher n_e than the true n_e, leading to the overestimation of F_{io}

For comparison, F_{re} and F_{io} are also inferred by using a uniform plasma slab model. The only difference from the SPM case is that n_e and T_e, are constant and the same procedure discussed for SPM is followed to calculate wavelength channel intensities. Figure 11(b) shows the relation between the inferred line-integrated recombination rates from the uniform slab model $F_{\mathrm{re,slab}}$ and the true values. Interestingly, good agreement is obtained even though the uniform slab model does not take into account the spatial variations of the plasma parameters. As discussed in section 2, recombination events per number photons due to recombination emission of the D_ϵ line are relatively insensitive to T_e and n_e in the ranges relevant to a divertor plasma. Hence, as long as the forward model reproduces the observed absolute intensity of D_ϵ, the inferred $F_{\mathrm{re,slab}}$ is reasonably close to the true value. On the other hand, figure 12(d) shows that the uniform slab model significantly underestimate F_{re} for data points with $I_\epsilon/I_\delta > 0.45$. In the cases shown in figure 12(e) and (f) where more lines are measured, F_{io} is systematically underestimated for $I_\epsilon/I_\delta > 0.45$. Moreover, $F_{\mathrm{io,slab}}$ has larger error bars than the corresponding $F_{\mathrm{io,SPM}}$. These results indicate that it is critical to model the spatial variations in the F_{io} inference.

5. Particle source and sink inference in an L-mode plasma

In this section, the analysis technique for particle source and sink inference is applied to an AUG L-mode discharge with N_2 seeding and a density ramp. Basic discharge parameters are shown in figures 14(a) and (b). This discharge has a lower single null configuration with the ion ∇B drift in the favorable direction. The edge safety fact q_{95} is 4 and the toroidal magnetic field B_t is 2.5 T. At $t = 1.6$ s, N_2 seeding starts and the D_2 puff amount increases at $t = 2.5$ and 3.5 s stepwise, leading to a gradual increase both in the core and edge $\bar{n}_e$. The external heating is only through electron cyclotron resonance heating (ECRH). The profiles of T_e, n_e and ion flux Γ_i on the outer divertor target are shown in figures 14(c), 14(d) and 14(e), respectively. Even with N_2 puffing and incremental D_2 fueling, the strong drops in n_e and Γ_i reported in Ref [5] are not observed. Thus, the outer divertor stays attached. However, after $t = 1.8$ s, T_e decreases and n_e increases significantly, indicating that the outer divertor plasma has entered the conduction-limited regime.

For this discharge, the line shapes of D_ϵ and D_δ are measured by using the lines of sight depicted in solid lines in figure 2. The line-integrated recombination and ionization rates (F_{re} and F_{io}) are inferred by using SPM. The analysis based on SPM is not applicable for $t < 2.3$ s due to insufficient D_ϵ and D_δ emission intensities. The profiles of I_ϵ and the I_ϵ/I_δ ratio along the outer divertor leg are shown in figures 15(a) and (b). The intersections between the lines of sight and the separatrix are assigned for each line of sight. Figures 15(c) and (d) show $F_{\mathrm{io,SPM}}$ and $F_{\mathrm{re,SPM}}$ along the divertor leg. The ionization rate increases as one moves away from the target. A large amount

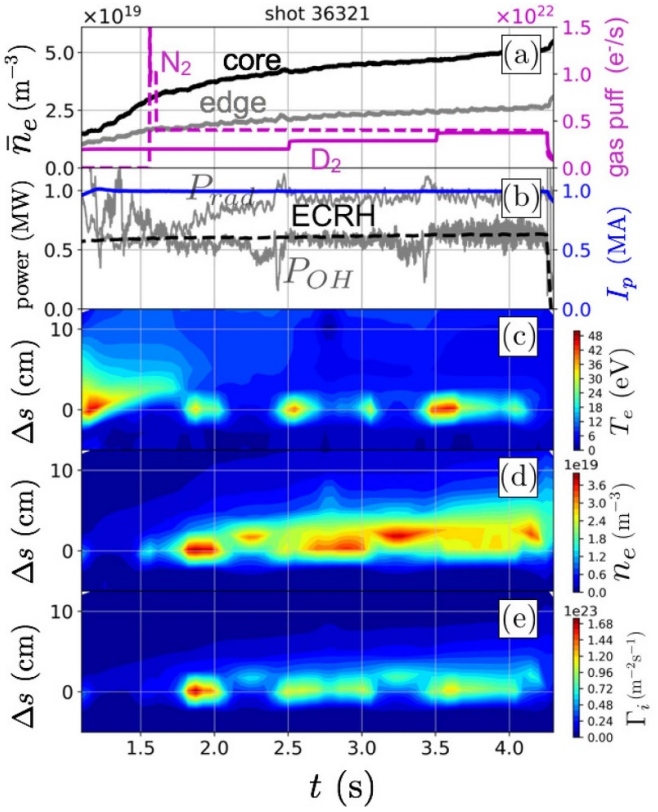

Figure 14. Time evolutions of basic plasma parameters. (a)Line-averaged n_e in the core and edge and gas puff rates. (b)Heating power (ECRH and Ohmic), radiated power and the plasma current. The profiles of T_e, n_e and ion flux Γ_i on the outer-divertor target are shown in (c), (d) and (e), respectively. Δs is the distance from the strike point. T_e, n_e and Γ_i are measured by the Langmuir probes shown in figure 3. Profiles shown in (c), (d) and (e) are created by linearly interpolating 9 spatial data points.

of ionization is expected in the upstream region, which is outside the coverage of lines of sight. It is important to note that the I_ϵ/I_δ ratio is above 0.45 for all points in time. Thus, as figure 12(b) indicates, the F_{io} inference has relatively large uncertainties for those I_ϵ/I_δ values while not shown. Recombination is localized near the strike point. The strong correlation between $F_{\mathrm{re,SPM}}$ and I_ϵ, which is expected from figure 4(a), is also observed. The profile of $\hat{n}_e$ (the average n_e in SPM) shown in figure 15(e) indicates that n_e monotonically increases as one approaches the strike point. Such n_e profiles are a feature of the conduction-limited regime.

The volume-integrated recombination rate and ionization rate are calculated by assigning the appropriate integration volumes for each line of sight. Figure 16 shows the volume-integrated recombination and ionization rates and the total ion flux on the outer divertor target. The particle source (volume integrated ionization) is reasonable for the high recycling regime given the expected additional contribution from the undiagnosted region. The particle sink (volume-integrated recombination) has a small contribution in the particle balance in this discharge. These observations are expected for the high-recycling regime where the particle influx from upstream is negligible in the particle balance.

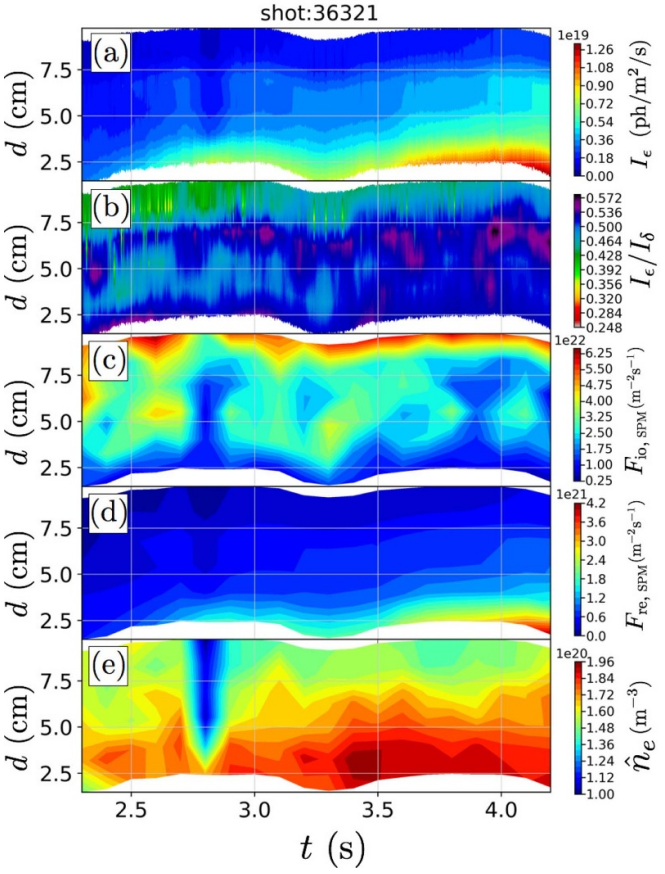

Figure 15. Time evolutions of plasma parameter profiles along the outer-divertor leg. d is the distance from the strike point in a poloidal cross-section. (a)D_ϵ emission intensity. (b)Ratio of D_ϵ emission intensity to D_δ emission intensity. (c)Line-integrated ionization rate inferred by the simplified profile model. (d)Line-integrated recombination rate inferred by the simplified profile model. (e) Average density $\hat{n}_e$ in the simplified profile model. These profiles are created by linearly interpolating 6 spatial data points.

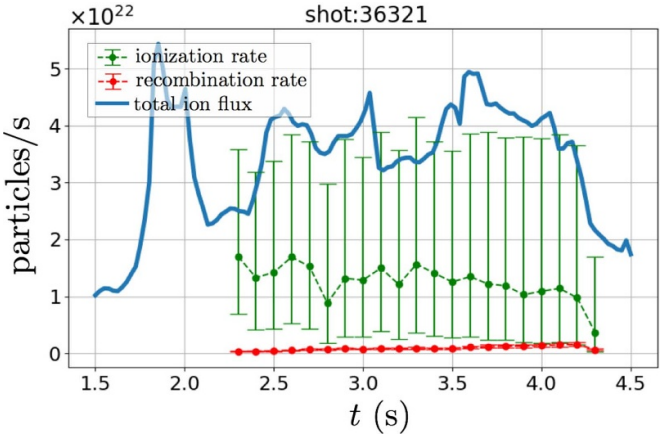

Figure 16. Particle balance in the outer divertor. The integrated volume is between the most upstream and most downstream lines of sight. The 50th percentiles of the probability distributions of line-integrated recombination and ionization rates are used for the data points. The upper and lower limits are estimated by using the 16th and 84th percentiles, respectively.

With the current diagnostic capability of AUG, only D_ϵ and D_δ can be measured simultaneously using the same line of sight. However, if a signal from one optical fiber is split and fed to two different spectrometers, the four Balmer lines D_ϵ, D_δ, D_γ and D_β can be measured simultaneously without sacrificing wavelength resolution. Optical fiber splitters are now under development and the F_{io} inference with higher precision will be possible in the near future at AUG.

6. Conclusions

A new analysis technique for Balmer line spectroscopy using Bayesian inference is presented. By comparing measured data and synthetic data calculated by a forward model, the new analysis technique utilizes all available information Balmer line spectroscopy provides: line broadening, line-ratios and absolute emission intensities. Moreover, the Bayesian framework allows for systematical inclusions of multiple Balmer lines in the analysis. This approach is especially useful for underdetermined problems, which Balmer line spectroscopy often encounters, since Bayesian inference provides constraints to the ranges of the parameters of interests by using prior knowledge about the plasma.

In order to measure line-integrated ionization and recombination rates in a closed divertor where spatial variations in the plasma parameters tend to be large, a simplified profile model (SPM) is developed as a forward model for the Bayesian inference. SPM is validated by using test data of D_ϵ, D_δ, D_γ and D_β spectra generated from SOLPS simulations. It is shown that SPM provides line-integrated ionization and recombination rates robustly over a wide parameter range. While line-integrated ionization rate inference using D_ϵ and D_δ lines have relatively large uncertainties especially when recombination emission dominates ($I_\epsilon/I_\delta > 0.45$), the precision improves significantly if D_γ and D_β are measured simultaneously.

SPM is also applied to D_ϵ and D_δ spectra obtained from an L-mode discharge in a high-recycling regime. The inferred ionization rate and recombination rate in the outer divertor volume is in a reasonable agreement with the expectations of the high recycling regime, providing further confidence in SPM.

Simultaneous four Balmer line (D_ϵ, D_δ, D_γ and D_β) measurements using the same line of sight will be available in the near future at ASDEX Upgrade and more precise inference of particle sink and source in a closed-divertor will be possible. In addition, the Bayesian framework allows this analysis technique to evolve to integrated data analysis for divertor plasmas [21]. Currently, a two dimensional forward model that utilizes additional lines of sight for Balmer spectroscopy, divertor Thomson scattering and Langmuir probes is under development. Such a model will be able to probe detailed structures of the divertor plasma parameters more reliably.

Acknowledgment

The authors would like to thank Dr M. D. Nornberg, Dr K. Verhaegh and Dr S. Kado for valuable discussions. This work has been carried out within the framework of the EUROfusion Consortium and has received funding from the Euratom research and training programme 2014-2018 and 2019-2020 under grant agreement No 633053. The views and opinions expressed herein do not necessarily reflect those of the European Commission.

Appendix A. Uncertainties in the absolute intensity calibration

Since the wavelength channels in a spectrometer share the same optics, the errors in the absolute intensities typically have a strong correlation between them. For example, when the absolute intensity of one wavelength channel is overestimated by 10%, it is likely that the other wavelength channels also suffer from the overestimation of the absolute intensities by near 10%. The likelihood given by equation(10) does not hold when σ_{λ_X}s are correlated to each other. Therefore, the uncertainties in the absolute intensities cannot simply be included in σ_{λ_X}. Assuming that all wavelength channels have the same relative error in the absolute intensities, equation (10) is rewritten:

$$\begin{aligned} p(\boldsymbol{D}|\theta, I) &= \prod_X \prod_{\lambda_X} \frac{1}{\sqrt{2\pi\sigma_{\lambda_X}^2/\iota^2}} \exp\left(-\frac{(I_{X,\lambda_X}/\iota - I_{X,\lambda_X}^{\mathrm{SPM}})^2}{2\sigma_{\lambda_X}^2/\iota^2}\right) \\ &= \iota \prod_X \prod_{\lambda_X} \frac{1}{\sqrt{2\pi\sigma_{\lambda_X}^2}} \exp\left(-\frac{(I_{X,\lambda_X} - \iota I_{X,\lambda_X}^{\mathrm{SPM}})^2}{2\sigma_{\lambda_X}^2}\right), \end{aligned} \tag{A1}$$

where ι represents the error in the absolute intensity, *e.g.*, when $\iota = 1.1$, the absolute intensities of all wavelength channels λ_Xs are overestimated by 10%. Note that σ_{λ_X} is also divided by ι since σ_{λ_X} is calculated by using the absolute intensity calibration. The leftmost ι in the second line of equation (A1) does not affect the ionization and recombination rate inference when the prior of ι is uniform. The second ι in the exponent modifies $I_{X,\lambda_X}^{\mathrm{SPM}}$. This form is identical to that of equation (10) when $\hat{l}$ is replaced by $\iota\hat{l}$:

$$\begin{aligned} \iota I_{X,\lambda_X}^{\mathrm{SPM}} &= \int d\lambda H_{\lambda_X}(\lambda) \int_0^{2\hat{l}} dl \cdot \iota i_X(\boldsymbol{\theta}) L_X(\boldsymbol{\theta}) \\ &= \int d\lambda H_{\lambda_X}(\lambda) \int_0^{2\iota\hat{l}} dl \cdot i_X(\boldsymbol{\theta}') L_X(\boldsymbol{\theta}'), \end{aligned} \tag{A2}$$

where $\boldsymbol{\theta}' = [\iota\hat{l}, \hat{\alpha}, \hat{n}_e, \hat{T}_{e,l}, \hat{T}_{e,h}, \hat{n}_0]$. Therefore, both the uncertainties in the width of the emission volume and in the absolute intensity calibration can be taken into account by $\hat{l}$ in SPM. When the prior of ι is not uniform, ι needs to be added to the elements of $\boldsymbol{\theta}$ and the likelihood is given by equation (A1).

ORCID iDs

T Nishizawa https://orcid.org/0000-0003-1804-2308
M Cavedon https://orcid.org/0000-0002-0013-9753
D Brida https://orcid.org/0000-0002-8647-7058

References

[1] Pitcher C S and Stangeby P C 1997 Experimental divertor physics *Plasma Phys. Control. Fusion* **39** 779–930
[2] Kallenbach A *et al* 2015 Partial detachment of high power discharges in ASDEX upgrade *Nucl. Fusion* **55** 053026
[3] Reimold F, Wischmeier M, Bernert M, Potzel S, Kallenbach A, Müller H W, Sieglin B, Stroth U and 2015 Divertor studies in nitrogen induced completely detached h-modes in full tungsten ASDEX upgrade *Nucl. Fusion* **55** 033004
[4] Potzel S, Dux R, Müller H W and Scarabosio A 2014 and M Wischmeier and. Electron density determination in the divertor volume of ASDEX upgrade via stark broadening of the balmer lines *Plasma Phys. Control. Fusion* **56** 025010
[5] Potzel S, Wischmeier M, Bernert M, Dux R, Müller H W, Scarabosio A and 2013 A new experimental classification of divertor detachment in ASDEX upgrade *Nucl. Fusion* **54** 013001
[6] Rosato J, Marandet Y and Stamm R 2017 A new table of balmer line shapes for the diagnostic of magnetic fusion plasmas *J. Quant. Spectrosc. Radiat. Transfer* **187** 333–7
[7] Lomanowski B A, Meigs A G, Sharples R M, Stamp M, Guillemaut C and 2015 Inferring divertor plasma properties from hydrogen balmer and paschen series spectroscopy in JET-ILW *Nucl. Fusion* **55** 123028
[8] Isler R C, McKee G R, Brooks N H, West W P, Fenstermacher M E and Wood R D 1997 Signatures of deuterium recombination in the diii-d divertor *Phys. Plasmas* **4** 2989–96
[9] Verhaegh K *et al* 2019 An improved understanding of the roles of atomic processes and power balance in divertor target ion current loss during detachment *Nucl. Fusion* **59** 126038
[10] Verhaegh K, Lipschultz B, Duval B P, Fil A, Wensing M, Bowman C, Gahle D S and 2019 Novel inferences of ionisation and recombination for particle/power balance during detached discharges using deuterium balmer line spectroscopy *Plasma Phys. Control. Fusion* **61** 125018
[11] Leonard A W 2018 Plasma detachment in divertor tokamaks *Plasma Phys. Control. Fusion* **60** 044001
[12] Summers H P 2004 *The ADAS User Manual* version 2. 6th edn
[13] Sakamoto M *et al* 2017 Molecular activated recombination in divertor simulation plasma on gamma 10/pdx *Nuclear Mater. Energy* **12** 1004–9 Proc. of the 22nd Int. Conf. on Plasma Surface Interactions 2016, 22nd PSI
[14] Terry J L, Lipschultz B, Pigarov A Y, Krasheninnikov S I, LaBombard B, Lumma D, Ohkawa H, Pappas D and Umansky M 1998 Volume recombination and opacity in alcator c-mod divertor plasmas *Phys. Plasmas* **5** 1759–66
[15] Kotov V, Reiter D, Kukushkin A S, Pacher H D, Börner P and Wiesen S 2006 Radiation absorption effects in b2-eirene divertor modelling *Contrib. Plasma Phys.* **46** 635–42
[16] Lomanowski B *et al* 2019 Spectroscopic investigation of n and ne seeded induced detachment in jet iter-like wall l-modes combining experiment and edge2d modeling *Nuclear Mater. Energy* **20** 100676
[17] Schneider R, Bonnin X, Borrass K, Coster D P, Kastelewicz H, Reiter D, Rozhansky V A and Braams B J 2006 Plasma edge physics with b2-eirene *Contrib. Plasma Phys.* **46** 3–191
[18] Reimold F, Wischmeier M, Potzel S, Guimarais L, Reiter D, Bernert M, Dunne M and Lunt T 2017 The high field side

high density region in solps-modeling of nitrogen-seeded h-modes in asdex upgrade *Nuclear Mater. Energy* **12** 193–9 Proc. of the 22nd Int. Conf. on Plasma Surface Interactions 2016, 22nd PSI

[19] Devinderjit Sivia and John Skilling 2006 *Data Analysis: a Bayesian Tutorial* (Oxford: Oxford University Press)

[20] Nornberg M D, Den Hartog D J and Reusch L M 2018 Incorporating beam attenuation calculations into an integrated data analysis model for ion effective charge *Fusion Sci. Technol.* **74** 144–53

[21] Fischer R, Fuchs C J, Kurzan B, Suttrop W and Wolfrum E 2010 and ASDEX Upgrade Team. Integrated data analysis of profile diagnostics at asdex upgrade *Fusion Sci. Technol.* **58** 675–84

[22] Nishizawa T, Nornberg M D, Den Hartog D J and Craig D 2016 Upgrading a high-throughput spectrometer for high-frequency (< 400 khz) measurements *Rev. Sci. Instrum.* **87** 11E530

[23] David J 2005 Earl and Michael W. Deem. Parallel tempering: Theory, applications, and new perspectives *Phys. Chem. Chem. Phys.* **7** 3910–16

[24] Foreman-Mackey D, Hogg D W, Lang D and Goodman J 2013 emcee: the mcmc hammer *Publ. Astron. Soc. Pac.* **125** 306